Facile synthesis of platinum–ruthenium nanodendrites supported on reduced graphene oxide with enhanced electrocatalytic properties

CrossMark

Jie-Ning Zheng [a], Shan-Shan Li [a], Fang-Yi Chen [a], Ning Bao [b], Ai-Jun Wang [a,*],
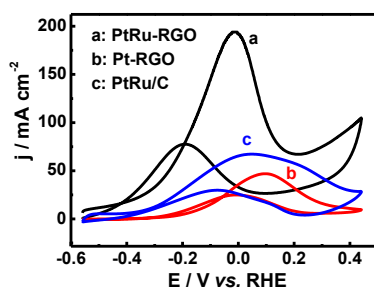Jian-Rong Chen [a], Jiu-Ju Feng [a,*]

[a] College of Chemistry and Life Science, College of Geography and Environmental Science, Zhejiang Normal University, Jinhua 321004, China
[b] School of Public Health, Nantong University, Nantong 226019, China

HIGHLIGHTS

- A facile strategy is developed for one-pot synthesis PtRu nanodendrites supported on RGO.
- HDPC as a shape-directing agent plays a vital role in formation of PtRu nanodendrites.
- The porous nanostructures show high electrochemically active surface area.
- The nanocomposites display excellent electrocatalytic performance towards EG oxidation.

GRAPHICAL ABSTRACT

ARTICLE INFO

ABSTRACT

In this report, a simple and facile solvothermal method is developed for fabrication of platinum–ruthenium (PtRu) nanodendrites supported on reduced graphene oxide (PtRu-RGO) in the ethylene glycol (EG) system, using hexadecylpyridinium chloride (HDPC) as a shape-directing agent. The as-prepared nanocomposites show the superior catalytic activity and better stability towards EG oxidation, compared with RGO-supported Pt nanoparticles and commercial PtRu/C (Pt 30 wt. %, Ru 15 wt. %) catalysts. This strategy may open a new route to design and prepare advanced electrocatalysts in direct EG fuel cells.

1. Introduction

Direct methanol fuel cells (DMFCs) are regarded as promising energy devices for many applications such as laptop computers, cellular phones and secondary electrical generators [1]. However, methanol has some disadvantages including high toxicity, flammability and tendency to crossover the fuel cell membrane, owing to its small molecular diameter [2]. As a result, many efforts have been made to develop alternative fuels. Ethylene glycol (EG) is considered as a potential fuel candidate next to methanol, because of its low toxicity, large volumetric energy density, and low volatility [3]. Although there are several examples using EG as a liquid fuel [4,5], electrooxidation of EG still remains less explored, compared with other alcohols.

* Corresponding authors. Tel./fax: +86 579 82282269.
E-mail addresses: ajwang@zjnu.cn, ajwangnju@gmail.com (A.-J. Wang), jjfeng@zjnu.cn (J.-J. Feng).

Pt nanostructures have been extensively investigated as electrocatalysts in fuel cells. However, their promising applications are usually hindered due to their easy poison by chemisorbed CO-like intermediates generated from the decomposition of alcohols [6,7]. Thus, much work has been focused on solving these problems by incorporating Pt with other metals such as Pd, Ag, Cu, Co, Fe, and Ru [8–13]. Among the bimetallic catalysts, PtRu catalysts exhibit the enhanced tolerance of CO and improved electrocatalytic activity [14–18], because Ru has the ability to facilitate the generation of oxygen-containing species at a relatively lower potential than that of Pt, and benefits CO oxidation on the adjacent active sites to form CO_2 [19].

It is known that a catalysis reaction usually occurs at the surface of a catalyst. Therefore, it is significant and practical to use a nanostructured catalyst with enlarged surface area for reducing the noble metal loading and improving its catalytic activity. To date, most of PtRu nanocrystals are solid structures with broad size distributions [20–25], which would reduce the catalytic efficiency.

Recently, porous nanostructures have attracted increasing interest for their superior electrocatalytic performance and lower noble-metal loading, which have high porosity, rich corner/edge atoms, and large specific surface area [26–30]. Although many porous nanostructures have been synthesized, most of the methods require severe reaction conditions such as seeds, hard templates, and complicated procedures. For example, Wang and co-workers synthesized porous PtCu nanoparticles using copper nanoparticles as a sacrificial template via a modified galvanic replacement approach [31]. In another example, Liu et al. prepared porous PdCu alloy via the replacement reaction between porous Cu and H_2PdCl_4 under N_2-protected conditions [32].

Another strategy is to load bimetallic catalysts onto the surface of carbon materials such as carbon black and carbon nanotubes. As a result, their catalytic, electrochemical and electrical properties are greatly improved [33,34]. Recently, graphene has attracted tremendous attention as a promising support in batteries, supercapacitors, fuel cells, photovoltaic devices, and biosensors [35], owing to its high electrical conductivity (10^5–10^6 S m^{-1}), extremely large specific surface area ($\sim$2630 m^2 g^{-1}), and superior chemical activity [36,37]. The residual oxygen-containing functional groups on graphene surface and its derivatives can be used as anchoring sites for metal nanoparticles [38]. Therefore, a variety of graphene supported metal catalysts have been fabricated and explored in catalysis reactions [13,39–42].

In this report, a simple and facile strategy was developed for preparation of highly porous PtRu nanodendrites on reduced graphene oxide (PtRu-RGO) in the EG system, using hexadecylpyridinium chloride (HDPC) as a shape-directing agent. The electrocatalytic activity and durability of the as-prepared PtRu-RGO were examined, using EG oxidation as a bench model system.

2. Experimental

2.1. Materials

Graphite powders (8000 meshes), chloroplatinic acid (H_2PtCl_6), ruthenium (III) chloride hydrate, hexadecylpyridinium chloride (HDPC), ethylene glycol (EG) were purchased from Aladdin chemistry Co., Ltd. Commercial PtRu/C (Pt 30 wt. %, Ru 15 wt. %) was supplied from Alfa Aesar. The other chemicals were analytical grade and used without further purification. All aqueous solutions were prepared with twice distilled water.

2.2. Synthesis of porous PtRu nanodendrites on reduced graphene oxide

For typical preparation of PtRu-RGO, GO was firstly prepared from natural graphite powder via the modified Hummer's method [43]. Then, 5 mL of GO (1 mg mL^{-1} in EG solution) and 450 mg of HDPC were dispersed in 25 mL of EG solution and ultrasonicated for 1 h, followed by simultaneously adding 10.36 mL of H_2PtCl_6 (19.31 mM) and 0.04149 g of $RuCl_3 \cdot H_2O$ into the mixture under stirring for another 1 h at ambient temperature. The pH of the mixed solution was adjusted to 11 by freshly prepared KOH solution (1.0 M), and then transferred to a Teflon-lined stainless autoclave and heated at 160 °C for 6 h. The final products were collected by centrifugation, and washed thoroughly with hot water.

For comparison, using individual H_2PtCl_6 and $RuCl_3 \cdot H_2O$ as a precursor, RGO supported Pt nanoparticles (Pt-RGO) and Ru nanoparticles (Ru-RGO) were prepared in a similar way, respectively, while other conditions were kept the same.

2.3. Electrochemical measurements

The electrochemical measurements were performed on a CHI832b electrochemical workstation (CH Instruments, Chenhua Co., Shanghai, China). A glassy carbon electrode (GCE, 3 mm in diameter), a coiled Pt wire, and Hg/HgO electrodes were used as the working electrode, counter electrode, and reference electrode, respectively.

For the construction of PtRu-RGO modified electrode, the PtRu-RGO suspension (2.94 mg mL^{-1}) was ultrasonicated for 30 min. Then, 6 μL of the suspension was dropped onto the electrode surface and dried in air, followed by casting 6 μL of Nafion (0.5 wt.%) on the electrode surface and allowed drying naturally. Similarly, Pt-RGO and commercial PtRu/C catalysts modified electrodes were prepared under the same conditions. The metal loading is around 0.20 mg cm^{-2} for these three catalysts modified electrodes.

The electrochemically active surface area (EASA) of a catalyst can be estimated via CO-stripping voltammograms in 1.0 M KOH. Meanwhile, the electrocatalytic activity and stability of PtRu-RGO modified electrode were determined by cyclic voltammetry and chronoamperometry towards EG oxidation in 1.0 M KOH, respectively. The current densities are normalized with respect to the geometrical area of the modified electrode.

2.4. Instrumental characterization

The structure and morphology of the products were characterized by transmission electron microscopy (TEM), high-resolution TEM (HRTEM), and high-angle annular dark-field scanning transmission electron microscopy (HAADF-STEM) measurements. TEM analysis was carried out on a JEM-2010HR TEM at an accelerating voltage of 200 kV, coupled with an energy-dispersive X-ray spectrometer (EDS, Dxford-1NCA) for detection of the average composition of elements in the products. The crystal structures were determined by X-ray diffraction (XRD, Rigaku Dmax–2000 diffractometer) employing Cu Kα radiation. The oxidation states of the catalysts were measured by K–Alpha X-ray photoelectron spectra (XPS) (ThermoFisher, E. Grinstead, UK) with an Al Kα X-ray radiation (1486.6 eV) for excitation. Fourier transform infrared (FT-IR) spectra were recorded in the form of KBr pellets with a Nicolet 670 FT-IR spectrometer. Raman spectra were acquired on a Renishaw Raman system model 1000 spectrometer equipped with a charge-coupled-device (CCD) detector, performed with a He/Ne laser at a wavelength of 633 nm. Thermogravimetric analysis (TGA) was carried out in air with a NETZSCH STA 449C thermogravimetric

analyzer. The samples were air-heated from room temperature to 900 °C at a rate of 10 °C min^{-1}.

3. Results and discussion

3.1. Characterization

Fig. 1(A) shows the low resolution TEM image of the as-synthesized products. There are many well-defined nano-dendrites with uniformly interconnected porous structures, which are evenly decorated on the RGO surface, with a narrow size distribution from 10 to 21 nm. The average size is around 15 nm. In addition, each nanodendrite is composed of many small particles with the diameter of 3−4 nm (Fig. 1(B)).

HRTEM image (Fig. 1(C)) displays that the nanoparticle is a porous dendritic entity with branches in different directions. The lattice fringes are coherently extended across over several branches, indicated by the arrows (Fig. 1(C)). The filtered images in the square area show that the d-spacings (0.23 nm and 0.20 nm) correspond to the (111) and (200) planes of the face centered cubic (fcc) PtRu structure. Fig. 2(A) shows the HAADF-STEM image of PtRu nanodendrite. The corresponding elemental mapping images (Fig. 2(B, C)) reveal homogeneous distribution of Pt and Ru elements throughout the whole nanodendrite, as strongly supported by the corresponding EDS analysis (Fig. 2(D)). The atomic ratio of Pt to Ru (Pt/Ru) is 87/13 in PtRu-RGO. For comparison, TEM image of commercial PtRu/C is also provided (Fig. 3). Notably, many tiny and slightly aggregated nanoparticles are distributed on the carbon.

Impressively, only using H_2PtCl_6 as a precursor yields large and irregular nanoparticles aggregated together under the same conditions (Fig. 4(A)). Similarly, it still fails to obtain nanodendrites just with $RuCl_3$ as a precursor (Fig. 4(B)). Additionally, the absence of HDPC induces the formation of smaller individual nanoparticles unevenly dispersed on RGO (Fig. 4(C)), revealing the critical role of HDPC in the present synthesis.

Fig. 5 illustrates the growth mechanism for porous PtRu nanodendrites. Their proposed formation mechanism may be ascribed to the particle attachment and self-aggregation of initially formed small branches using HDPC as shape-directing agent [26]. The lattice fringes of PtRu nanodendrites are perfectly aligned along the arrows (Fig. 1(C)), indicating that they are formed by the oriented attachment mechanism. However, the domain boundaries are clearly observed (Fig. 1(C)), which can be attributed to the involvement of twinning and/or imperfect oriented attachment characterized by a small misorientation at the interface [44].

The XRD pattern demonstrates good crystallinity of PtRu nanocrystals in PtRu-RGO (Fig. 6, curve a), where the representative diffraction peaks at 39.9°, 46.3°, 67.8°, and 81.4° are matched well with the (111), (200), (220), and (311) crystal planes of fcc Pt, as also confirmed by the XRD pattern of the Pt-RGO sample (curve b). The 2θ values of PtRu-RGO slightly shift to higher angles than those of Pt-RGO, owing to the incorporation of Ru atoms into Pt lattices [45]. The average crystallite size of PtRu primary nanoparticles is 8.3 nm, calculated from the peak width of the (111) diffraction according to the Scherrer's equation [46]. Note that the particle size is larger than that obtained from the TEM analysis (Fig. 1(B)), which might
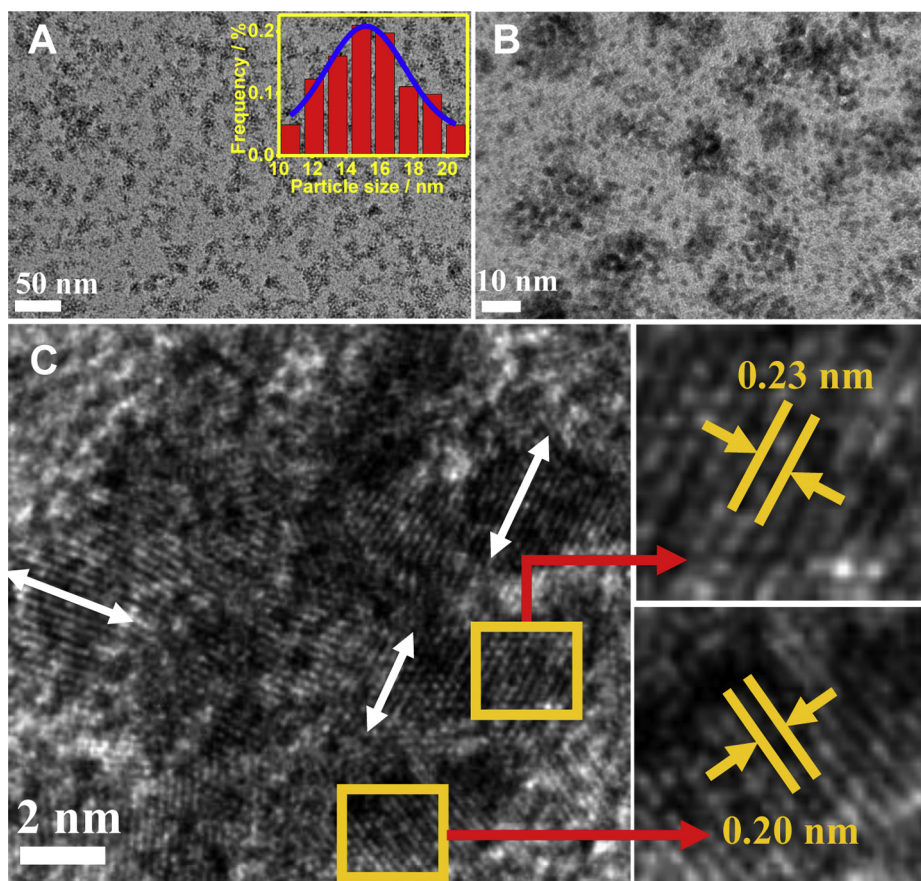

Fig. 1. TEM (A−B) and HRTEM (C) images of the PtRu-RGO sample. Inset shows the size distribution in image (A).
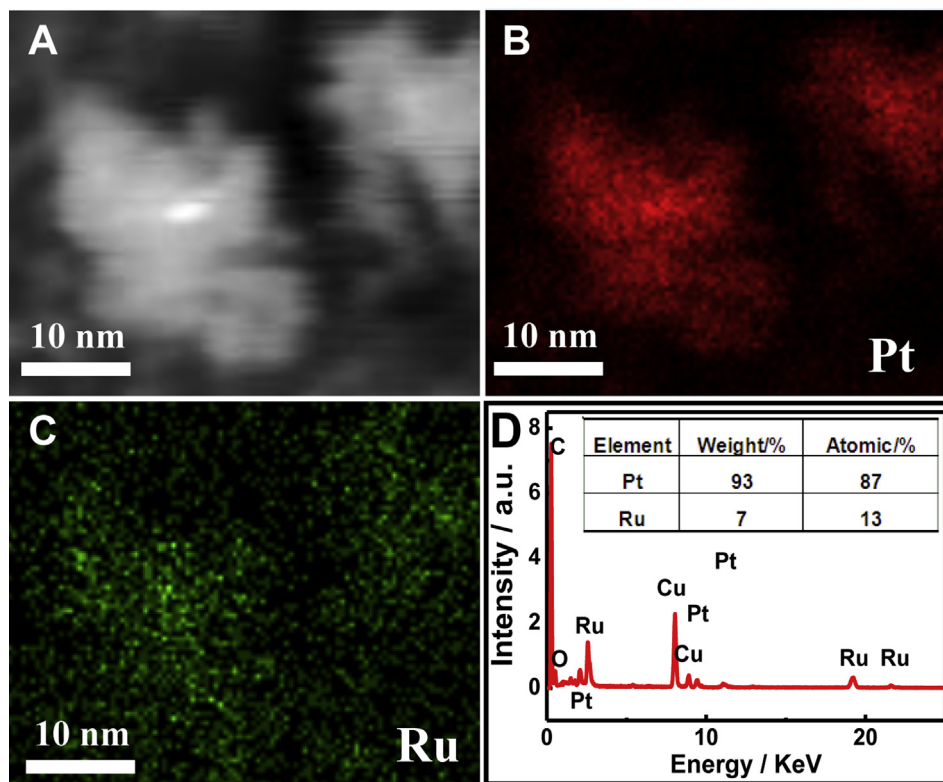
Fig. 2. HAADF-STEM image (A), elemental mapping images of Pt (B) and Ru (C), and EDS pattern (D) of PtRu-RGO.

be ascribed to the oriented attachment of the primary crystallites in the hierarchical nanoparticles [47].

Moreover, the diffraction peak at 21.7° is assigned to the (002) planes of hexagonal structure of graphene, which is different from the GO sample (curve c) with a diffraction peak at 10.5° corresponding to the oxygenated functional groups [48]. It indicates that GO is completely reduced to RGO by EG and the reestablishment of the conjugated graphene network (sp² carbon) [49,50]. The XRD analysis provides solid evidence for synthesis of PtRu-RGO.

XPS is a powerful tool to characterize the valence states and surface composition of nanomaterials. As illustrated in Fig. 7(A), the XPS survey spectrum of PtRu-RGO is dominated by the signals of Pt, Ru, C, N, and O elements. The peaks at 75.3 eV and 72.1 eV are assigned to Pt $4f_{5/2}$ and Pt $4f_{7/2}$ (Fig. 7(B)), respectively. To identify the valence states of Pt, the spectrum can be divided into two pairs

Fig. 3. TEM image of commercial PtRu/C.

of Lorentzian curves. The stronger peaks at 75.28 and 72.03 eV are attributed to Pt^0, while the weaker ones located at 76.48 and 73.08 eV correspond to Pt^{2+} in PtO or $Pt(OH)_2$ [20]. From the intensity of these peaks, we can conclude that Pt^0 is the predominant species.

Similar method is used to analyze Ru valence states (Fig. 7(C)). As the Ru 3d peaks overlap with the C 1s peak, the Ru $3p_{3/2}$ spectrum is chosen for analysis, which appears at around 462.7 eV. This peak is further separated into three peaks at 466.48, 463.98, and 462.18 eV, corresponding to Ru^0, oxidized Ru, and hydrated Ru oxide species [51], respectively. Obviously, Ru^0 is the main species. Additionally, the peak at 285.0 eV is attributed to the binding energy of C 1s (Fig. 7(D)), which is fitted into three peaks at 284.98, 285.83, and 286.48 eV, corresponding to C–C (sp^2), C–O, and C=O, respectively [52]. Table 1 provides the corresponding binding energy and the component content in PtRu-RGO. XPS analysis demonstrates the formation of PtRu nanoparticles on RGO.

Fig. 8(A) shows the FT-IR spectra of PtRu-RGO (curve a) and GO (curve b). For GO, the characteristic peaks at 1040, 1230, 1400, and 1740 cm^{-1} are observed, which are originated from the C–OH stretching, C–O stretching, O–H stretching, and C=O stretching groups [53]. However, most of the peaks from the oxygen-containing groups greatly decrease, probably owing to the formation of RGO.

Furthermore, Raman spectroscopy is another useful tool to monitor structural changes of graphene. Typical Raman spectra of PtRu-RGO and GO show two distinguished characteristic peaks at 1351 and 1596 cm^{-1} (Fig. 8(B)), corresponding to the D band related with the A_{1g} breathing mode of disordered graphite structure and G band associated with the doubly degenerate E_{2g} of graphite [54]. The integral area ratio of the two bands (I_D/I_G) is 1.37 for PtRu-RGO, which is much larger than that of GO (0.82). It is known that this
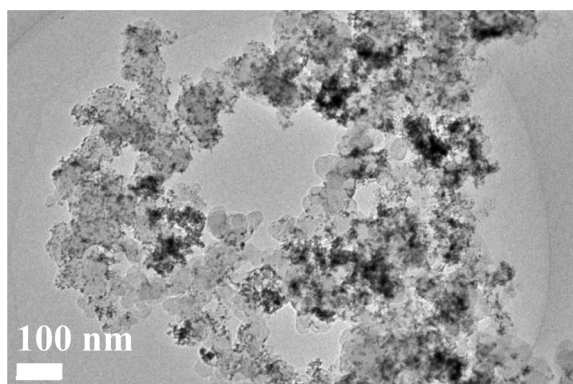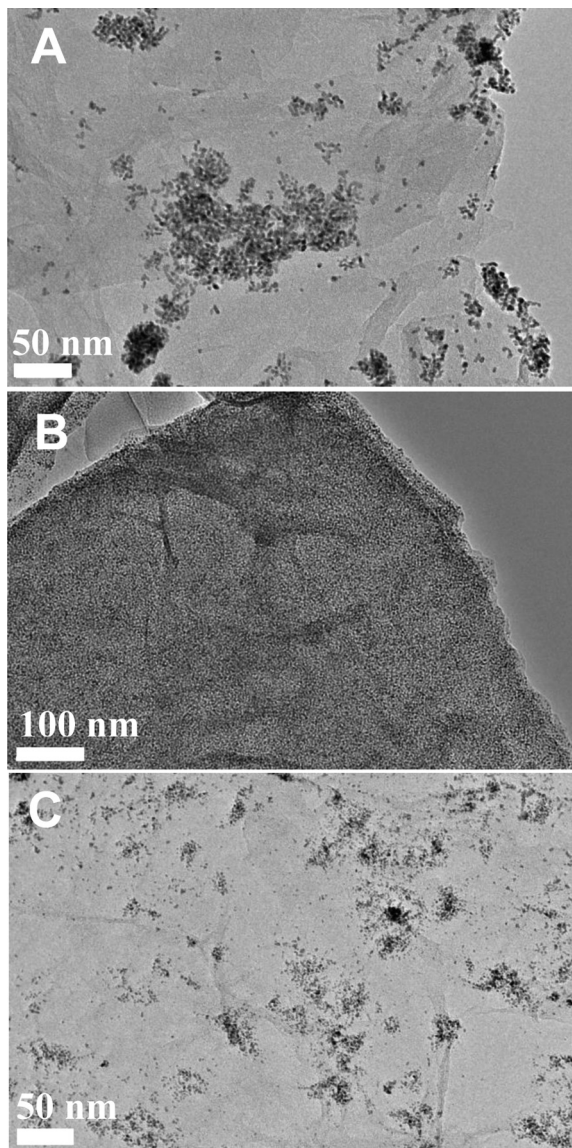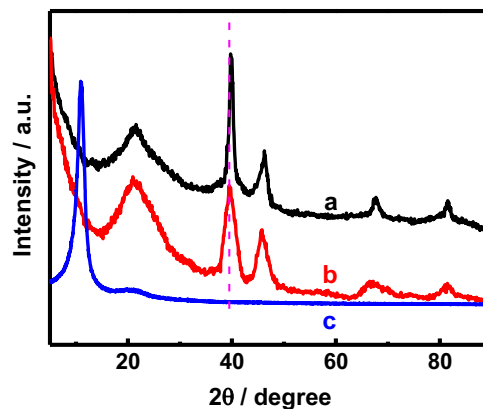
Fig. 6. XRD patterns of PtRu-RGO (curve a), Pt-RGO (curve b), and GO (curve c).

value is inversely proportional to the in-plane crystallite size of graphitic materials [55]. The larger value of the I_D/I_G shows good preservation of the highly crystalline structure of graphene [56], which is essential to achieve good electrical conductivity in the hybrid composites.

TGA analysis was conducted to investigate the weight loss of porous PtRu-RGO (Fig. 9, curve a). The weight loss within 100 °C comes from the escape of water molecules adsorbed between RGO nanosheets. The distinguished weight loss is much lower in the temperature range of 138–200 °C, similar to that of Pt-RGO (curve b) but different from that of GO (curve c) under the identical conditions, showing the decreased quantity of the oxygen-containing functional groups on RGO. Additionally, the metal mass loading is evaluated to be 76.7% for PtRu-RGO, and 54.4% for Pt-RGO, respectively.

3.2. Electrochemical properties

The electrochemically active surface area (EASA) is closely related to the number of available active sites. In this work, the EASA of PtRu-RGO is around 59.62 m^2 g^{-1} metal by CO-stripping voltammetry (Fig. 10(A)). This value is larger than those of Pt-RGO (29.53 m^2 g^{-1} metal, Fig. 10(B)) and commercial PtRu/C (55.66 m^2 g^{-1} metal, Fig. 10(C)) catalysts, owing to porous PtRu nanodendrites with the narrow distribution on RGO. Moreover, the

Fig. 4. TEM images of Pt-RGO (A), Ru-RGO (B), and PtRu-RGO obtained without HDPC (C).
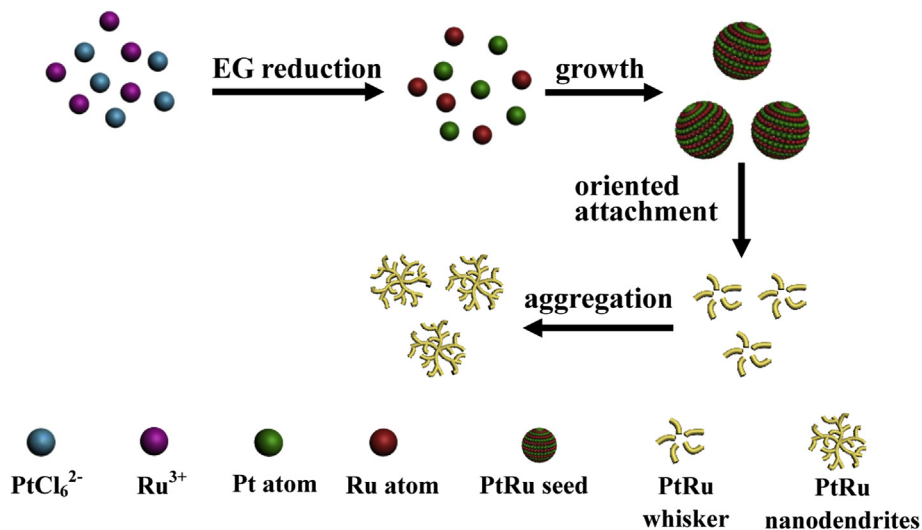

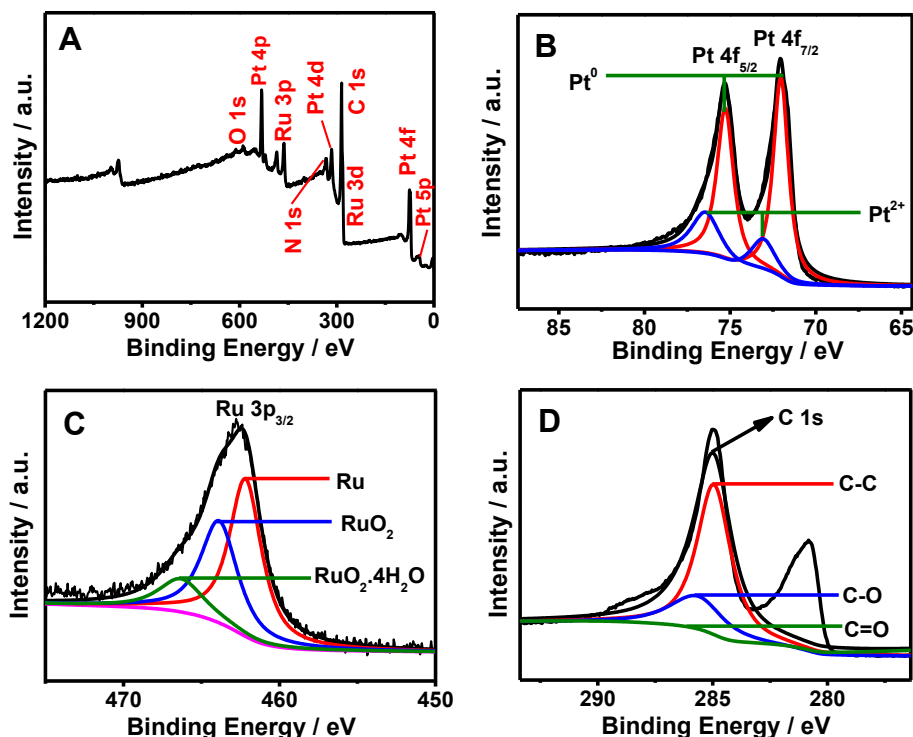**Fig. 5.** The formation mechanism for porous PtRu nanodendrites.

Fig. 7. XPS survey spectra of PtRu-RGO (A), high-resolution XPS spectra of Pt $4f_{7/2}$, Pt $4f_{5/2}$ (B), Ru $3p_{3/2}$ (C), and C 1s (D).

onset potential is −0.285 V for PtRu-RGO, which is negative than those of Pt-RGO (−0.260 V) and commercial PtRu/C (−0.266 V) catalysts. The larger EASA and negative shift of the onset potential are very important to the electrocatalytic performance of PtRu-RGO.

Fig. 11(A) shows the cyclic voltammetric behaviors of PtRu-RGO (curve a), Pt-RGO (curve b), and commercial PtRu/C (curve c) catalysts modified electrodes in 1.0 M KOH containing 1.0 M EG. In each case, an EG oxidation peak is clearly detected in the forward scan from −0.1 to 0.1 V. And another anodic peak is emerged during the reverse scan, corresponding to the removal of incompletely oxidized carbonaceous species (e.g. CO) produced in the forward scan. Moreover, the current density increases in the forward scan because higher potential promotes EG oxidation. And more positive potential induces surface oxidation of the metal nanoparticles, resulting in their decreased activity and current density. In the backward scan, the catalyst is regenerated via the reduction of the oxidized surface, leading to a jump in current density, followed by the current decrease as the potential goes down [57,58]. The corresponding maximum catalytic currents were normalized with the EASA and the loading amount of metals.

As shown in Fig. 11(B), the specific activity of PtRu-RGO modified electrode is 1.71 mA cm^{-2} metal, which is about 2.06 and 2.71 times higher than those of Pt-RGO (0.83 mA cm^{-2} metal) and commercial PtRu/C (0.63 mA cm^{-2} metal) catalysts modified electrodes. Besides, the mass activity is 1058.90 mA mg^{-1} metal for PtRu-RGO, which is 4.31 and 3.01 times over those of Pt-RGO (245.72 mA mg^{-1} metal) and commercial PtRu/C (352.01 mA mg^{-1} metal) catalysts.

The ratio of the forward oxidation peak current density (j_f) to the reverse oxidation peak current density (j_r), j_f/j_r, is usually used to check the tolerance of a catalyst to the accumulation of incompletely oxidized species [22]. A high ratio of j_f/j_r indicates very efficient oxidation of EG to CO_2 and the removal of poisoning species from the catalyst surface. The j_f/j_r is 2.74 for PtRu-RGO, which is higher than those of Pt-RGO (1.89) and commercial PtRu/C (2.12) catalysts, indicating that PtRu-RGO suffers little from poisoning and deactivation. This is ascribed to more effective suppression of CO poisoning of PtRu-RGO.

It is well known that oxygen-containing groups such as OH$_{ads}$ have the ability to promote the oxidation of CO-like intermediates adsorbed on Pt active sites [59]. This would facilitate the regeneration of Pt active sites and improve electrocatalytic activity of Pt [60]. As to PtRu-RGO, the alloyed Ru and surface defects (functionalized groups) of RGO can more effectively remove the CO-like intermediates adsorbed on Pt active sites via the facile formation of Ru(OH)$_{ads}$ or RGO(OH)$_{ads}$ at the lower potential [59,61]. As a result, PtRu-RGO has the relatively strong CO-tolerance, compared with Pt-RGO and commercial PtRu/C.

Chronoamperometry is employed to examine the electrocatalytic stability of PtRu-RGO (Fig. 12, curve a), Pt-RGO (Fig. 12, curve b) and commercial PtRu/C (Fig. 12, curve c) catalysts modified electrodes in 1.0 M KOH + 1.0 M EG at an applied potential of 0.1 V for 6000 s. The polarization current of porous PtRu-RGO modified electrode greatly decreases within 1800 s, followed by the slow decay within 3300 s to approach a limiting current (up to
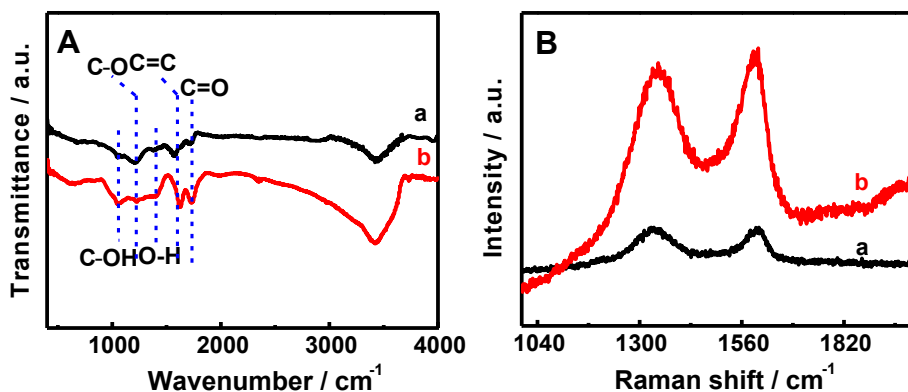
Table 1
XPS analysis of the binding energy and content of the components in PtRu-RGO.

Sample	Component	Binding energy/eV	Content/%
PtRu-RGO	Pt^0	75.28, 72.03	60.2
	Pt^{2+}	76.48, 73.08	39.8
	Ru^0	466.48	39.1
	RuO$_2$	463.98	35.3
	RuO$_2$·4H$_2$O	462.18	25.6
	C−C	284.98	57.9
	C−O	285.83	28.7
	C=O	286.48	13.4

Fig. 8. (A) FT-IR spectrum of PtRu-RGO (curve a) and GO (curve b). (B) Raman spectra of PtRu-RGO (curve a) and GO (curve b).

6000 s). The initial current density decreases quickly within 1800 s, possibly due to the absorbed poisonous intermediate species during the EG oxidation reaction [58]. Moreover, the limiting current density of PtRu-RGO modified electrode decreases to 10.89 mA cm^{-2} up to 6000 s, higher than those of Pt-RGO and commercial PtRu/C catalysts. The strong tolerance and improved stability of PtRu-RGO are attributed to the special structures of highly porous PtRu-RGO.

The improved electrocatalytic performance of PtRu-RGO is attributed to the following reasons: (i) The synergistic effects between Pt and Ru. The alloyed Ru can decrease the electronic binding energy in Pt and facilitate the C−H cleavage reaction at relatively low potential [11], and thus improve the electrocatalytic activity towards EG oxidation. The additional Ru can also remove CO adsorbed on Pt at a lower potential via facile formation of Ru(OH)$_{ads.}$ (ii) The porous structure contributes the bigger specific surface area. And the abundant atomic steps, edges, and corner atoms in PtRu branches would act as highly active sites for EG oxidation [62−64]. (iii) Better dispersion of PtRu nanodendrites on RGO that enlarges surface area and facilitates electron transport.

4. Conclusion

In summary, a simple and facile strategy was developed for synthesis of RGO-supported porous PtRu nanodendrites under solvothermal conditions, using HDPC as a shape-directing agent and EG as a reducing agent. PtRu-RGO exhibits the enhanced
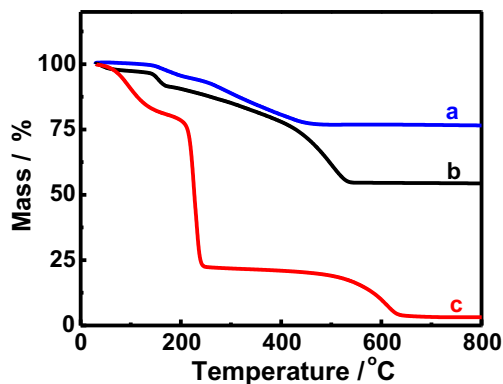

Fig. 9. Thermogravimetric analysis (TGA) of PtRu-RGO (curve a), Pt-RGO (curve b), and pure GO (curve c).
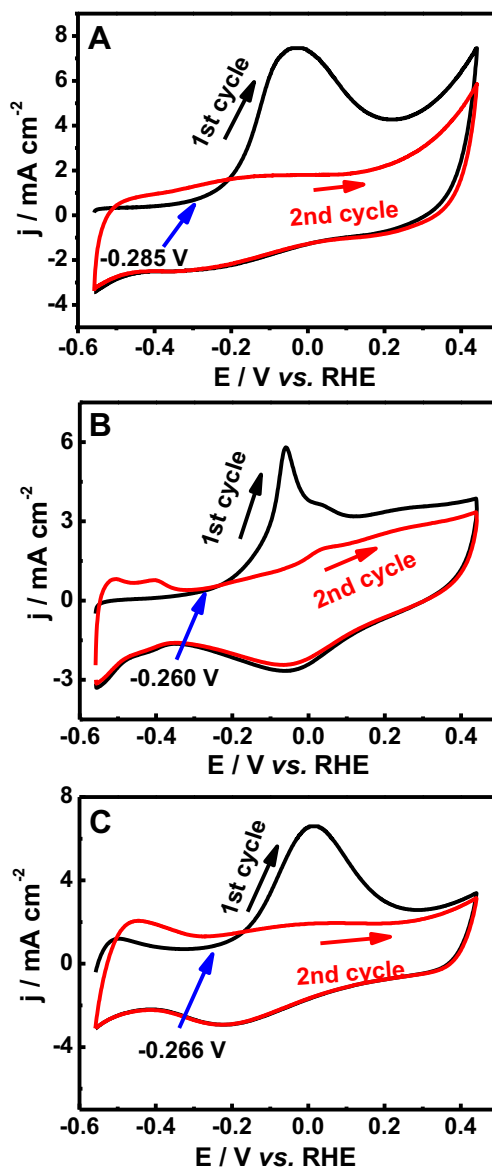

Fig. 10. CO-stripping voltammograms of PtRu-RGO (A), Pt-RGO (B), and commercial PtRu/C (C) catalysts modified electrodes in 1.0 M KOH at 50 mV s^{-1}.
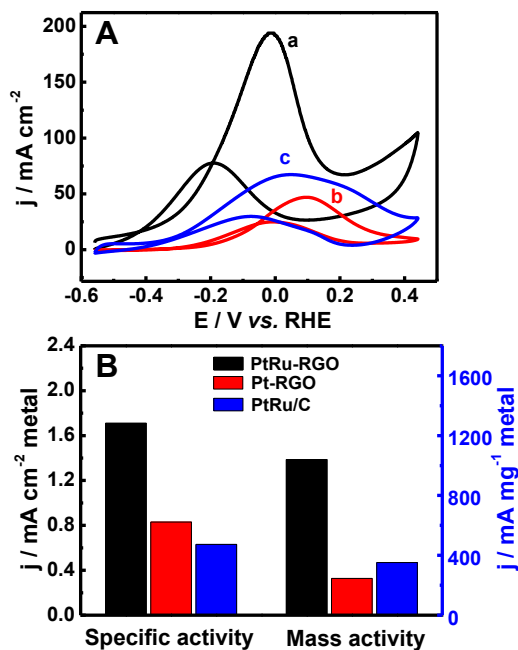
Fig. 11. Cyclic voltammograms of PtRu-RGO (curve a), Pt-RGO (curve b), and commercial PtRu/C (curve c) catalysts modified electrodes in 1.0 M KOH + 1.0 M EG at 50 mV s^{-1} (A). The corresponding specific and mass activities of these catalysts at peak potentials (B).
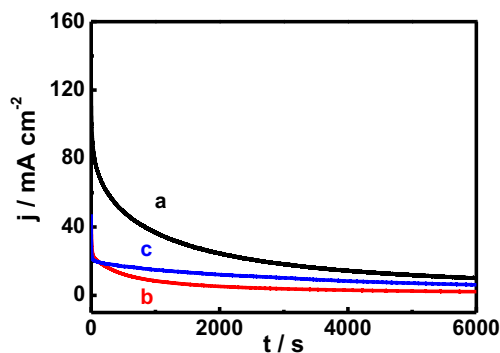

Fig. 12. Chronoamperometric curves of PtRu-RGO (curve a), Pt-RGO (curve b), and commercial PtRu/C (curve c) catalysts modified electrodes in 1.0 M KOH + 1.0 M EG solution at the applied potential of 0.1 V.

catalytic ability and improved stability towards EG oxidation, making it a promising catalyst in direct EG fuel cells. This work provides a new method for preparation of porous bimetallic nanostructure supported on RGO with an excellent catalytic activity.

Acknowledgment

References

[1] J.M. Sieben, M.M.E. Duarte, Int. J. Hydrogen Energy 36 (2011) 3313–3321.
[2] C. Jin, Y. Song, Z. Chen, Electrochim. Acta 54 (2009) 4136–4140.
[3] M. Chatterjee, A. Chatterjee, S. Ghosh, I. Basumallick, Electrochim. Acta 54 (2009) 7299–7304.
[4] K. Matsuoka, Y. Iriyama, T. Abe, M. Matsuoka, Z. Ogumi, J. Power Sources 150 (2005) 27–31.
[5] K. Miyazaki, T. Matsumiya, T. Abe, H. Kurata, T. Fukutsuka, K. Kojima, Z. Ogumi, Electrochim. Acta 56 (2011) 7610–7614.
[6] H. Ataee-Esfahani, L. Wang, Y. Nemoto, Y. Yamauchi, Chem. Mater. 22 (2010) 6310–6318.
[7] T. Li, H. You, M. Xu, X. Song, J. Fang, ACS Appl. Mater. Interfaces 4 (2012) 6942–6948.
[8] L. Wang, Y. Nemoto, Y. Yamauchi, J. Am. Chem. Soc. 133 (2011) 9674–9677.
[9] Y.-Y. Feng, J.-H. Ma, G.-R. Zhang, G. Liu, B.-Q. Xu, Electrochem. Commun. 12 (2010) 1191–1194.
[10] X. Yu, D. Wang, Q. Peng, Y. Li, Chem. Commun. 47 (2011) 8094–8096.
[11] L. Liu, E. Pippel, R. Scholz, U. Gösele, Nano Lett. 9 (2009) 4352–4358.
[12] D. Xiang, L. Yin, J. Mater. Chem. 22 (2012) 9584–9593.
[13] C. Nethravathi, E.A. Anumol, M. Rajamathi, N. Ravishankar, Nanoscale 3 (2011) 569–571.
[14] B.A. Kakade, T. Tamaki, H. Ohashi, T. Yamaguchi, J. Phys. Chem. C 116 (2012) 7464–7470.
[15] M.-L. Lin, M.-Y. Lo, C.-Y. Mou, Catal. Today 160 (2011) 109–115.
[16] R. Liu, H. Iddir, Q. Fan, G. Hou, A. Bo, K.L. Ley, E.S. Smotkin, Y.E. Sung, H. Kim, S. Thomas, A. Wieckowski, J. Phys. Chem. B 104 (2000) 3518–3531.
[17] M. Watanabe, M. Uchida, S. Motoo, J. Electroanal. Chem. Interfacial Electrochem. 229 (1987) 395–406.
[18] G.J.K. Acres, J.C. Frost, G.A. Hards, R.J. Potter, T.R. Ralph, D. Thompsett, G.T. Burstein, G.J. Hutchings, Catal. Today 38 (1997) 393–400.
[19] A. Chen, P. Holt-Hindle, Chem. Rev. 110 (2010) 3767–3804.
[20] R. Chetty, S. Kundu, W. Xia, M. Bron, W. Schuhmann, V. Chirila, W. Brandl, T. Reinecke, M. Muhler, Electrochim. Acta 54 (2009) 4208–4215.
[21] S.-Y. Huang, C.-T. Yeh, J. Power Sources 195 (2010) 2638–2643.
[22] T. Maiyalagan, T.O. Alaje, K. Scott, J. Phys. Chem. C 116 (2011) 2630–2638.
[23] W. Li, X. Wang, Z. Chen, M. Waje, Y. Yan, J. Phys. Chem. B 110 (2006) 15353–15358.
[24] P. Sivakumar, V. Tricoli, Electrochim. Acta 51 (2006) 1235–1243.
[25] F. Li, K.-Y. Chan, H. Yung, C. Yang, S.W. Ting, Phys. Chem. Chem. Phys. 15 (2013) 13570–13577.
[26] B. Lim, Y. Xia, Angew. Chem. Int. Ed. 50 (2011) 76–85.
[27] J. Chen, B. Lim, E.P. Lee, Y. Xia, Nano Today 4 (2009) 81–95.
[28] B.Y. Xia, W.T. Ng, H.B. Wu, X. Wang, X.W. Lou, Angew. Chem. Int. Ed. 51 (2012) 7213–7216.
[29] S.-S. Li, J.-J. Lv, Y.-Y. Hu, J.-N. Zheng, J.-R. Chen, A.-J. Wang, J.-J. Feng, J. Power Sources 247 (2014) 213–218.
[30] A.-J. Wang, F.-F. Li, J.-N. Zheng, H.-X. Xi, Z.-Y. Meng, J.-J. Feng, RSC Adv. 3 (2013) 10355–10362.
[31] M. Wang, W. Zhang, J. Wang, A. Minett, V. Lo, H. Liu, J. Chen, J. Mater. Chem. A 1 (2013) 2391–2394.
[32] A. Liu, H. Geng, C. Xu, H. Qiu, Anal. Chim. Acta 703 (2011) 172–178.
[33] Z. Zeng, X. Zhou, X. Huang, Z. Wang, Y. Yang, Q. Zhang, F. Boey, H. Zhang, Analyst 135 (2010) 1726–1730.
[34] B. Li, C.F. Goh, X. Zhou, G. Lu, H. Tantang, Y. Chen, C. Xue, F.Y.C. Boey, H. Zhang, Adv. Mater. 20 (2008) 4873–4878.
[35] C. Tan, X. Huang, H. Zhang, Mater. Today 16 (2013) 29–36.
[36] X. Huang, X. Qi, F. Boey, H. Zhang, Chem. Soc. Rev. 41 (2012) 666–686.
[37] X. Huang, Z. Yin, S. Wu, X. Qi, Q. He, Q. Zhang, Q. Yan, F. Boey, H. Zhang, Small 7 (2011) 1876–1902.
[38] C. Xu, X. Wang, J. Zhu, J. Phys. Chem. C 112 (2008) 19841–19845.
[39] M. Zhu, P. Chen, M. Liu, ACS Nano 5 (2011) 4529–4536.
[40] X. Huang, X. Zhou, S. Wu, Y. Wei, X. Qi, J. Zhang, F. Boey, H. Zhang, Small 6 (2010) 513–516.
[41] J. Chai, F. Li, Y. Hu, Q. Zhang, D. Han, L. Niu, J. Mater. Chem. 21 (2011) 17922–17929.
[42] J.-J. Lv, S.-S. Li, J.-N. Zheng, A.-J. Wang, J.-R. Chen, J.-J. Feng, Int. J. Hydrogen Energy 39 (2014) 3211–3218.
[43] W.S. Hummers, R.E. Offeman, J. Am. Chem. Soc. 80 (1958), 1339–1339.
[44] R.L. Penn, J.F. Banfield, Science 281 (1998) 969–971.
[45] X. Teng, S. Maksimuk, S. Frommer, H. Yang, Chem. Mater. 19 (2006) 36–41.
[46] C. Venkateswara Rao, C.R. Cabrera, Y. Ishikawa, J. Phys. Chem. C 115 (2011) 21963–21970.
[47] L. Zhang, J. Zhang, Z. Jiang, S. Xie, M. Jin, X. Han, Q. Kuang, Z. Xie, L. Zheng, J. Mater. Chem. 21 (2011) 9620–9625.
[48] H.-K. Jeong, Y.P. Lee, R.J.W.E. Lahaye, M.-H. Park, K.H. An, I.J. Kim, C.-W. Yang, C.Y. Park, R.S. Ruoff, Y.H. Lee, J. Am. Chem. Soc. 130 (2008) 1362–1366.
[49] Y. Li, W. Gao, L. Ci, C. Wang, P.M. Ajayan, Carbon 48 (2010) 1124–1130.
[50] S. Sharma, A. Ganguly, P. Papakonstantinou, X. Miao, M. Li, J.L. Hutchison, M. Delichatsios, S. Ukleja, J. Phys. Chem. C 114 (2010) 19459–19466.
[51] R.K. Raman, A.K. Shukla, A. Gayen, M.S. Hegde, K.R. Priolkar, P.R. Sarode, S. Emura, J. Power Sources 157 (2006) 45–55.
[52] L. Gao, W. Yue, S. Tao, L. Fan, Langmuir 29 (2012) 957–964.
[53] R. Bissessur, P.K.Y. Liu, W. White, S.F. Scully, Langmuir 22 (2006) 1729–1734.
[54] H.-L. Guo, X.-F. Wang, Q.-Y. Qian, F.-B. Wang, X.-H. Xia, ACS Nano 3 (2009) 2653–2659.
[55] M.A. Pimenta, G. Dresselhaus, M.S. Dresselhaus, L.G. Cancado, A. Jorio, R. Saito, Phys. Chem. Chem. Phys. 9 (2007) 1276–1290.
[56] F. Li, Y. Guo, R. Li, F. Wu, Y. Liu, X. Sun, C. Li, W. Wang, J. Gao, J. Mater. Chem. A 1 (2013) 6579–6587.

[57] Y. Liu, M. Chi, V. Mazumder, K.L. More, S. Soled, J.D. Henao, S. Sun, Chem. Mater. 23 (2011) 4199—4203.

[58] V. Mazumder, M. Chi, M.N. Mankin, Y. Liu, Ö. Metin, D. Sun, K.L. More, S. Sun, Nano Lett. 12 (2012) 1102—1106.

[59] J. Chen, M. Wang, B. Liu, Z. Fan, K. Cui, Y. Kuang, J. Phys. Chem. B 110 (2006) 11775—11779.

[60] J.-N. Zheng, J.-J. Lv, S.-S. Li, M.-W. Xue, A.-J. Wang, J.-J. Feng, J. Mater. Chem. A 2 (2014) 3445—3451.

[61] V. Selvaraj, M. Alagar, Electrochem. Commun. 9 (2007) 1145—1153.

[62] Z.-Y. Zhou, Z.-Z. Huang, D.-J. Chen, Q. Wang, N. Tian, S.-G. Sun, Angew. Chem. Int. Ed. 49 (2010) 411—414.

[63] S.W. Lee, S. Chen, W. Sheng, N. Yabuuchi, Y.-T. Kim, T. Mitani, E. Vescovo, Y. Shao-Horn, J. Am. Chem. Soc. 131 (2009) 15669—15677.

[64] M.A. Mahmoud, C.E. Tabor, M.A. El-Sayed, Y. Ding, Z.L. Wang, J. Am. Chem. Soc. 130 (2008) 4590—4591.